eprints@whiterose.ac.uk
https://eprints.whiterose.ac.uk/

Multiscale characterisation of the mechanical properties of austenitic stainless steel joints

P. Efthymiadis[1], R. Dashwood[1], B. Shollock[1], L. Curry[1], H. Ghadbeigi[2], A. Barrow[3], D Roberston[3]

[1]WMG, Warwick University, Coventry, CV4 7AL, UK
[2]Department of Mechanical Engineering, the University of Sheffield, Mappin Street, Sheffield S1 3JD, UK
[3] Rolls Royce PLC, Derby, DE21 7XX, UK
[*]Corresponding author: P.Efthymiadis@warwick.ac.uk, Tel: 0044 (0) 2476572528

Abstract

A multiscale investigation was pursued in order to obtain the strain distribution and evolution during tensile testing both at the macro- and micro-scale for a diffusion bonded 316L stainless steel. The samples were designed for the purpose to demonstrate that the bond line properties were equal or better than the parent material in a sample geometry that was extracted from a larger component. The macroscopic stress-strain curves were coupled to the strain distributions using a camera-based 2D - Digital Image Correlation system. Results showed significant amount of plastic deformation predominantly concentrated in shear bands which were extended over a large region, crossing through the joint area. Yet it was not possible to be certain whether the joint has shown significant plastic deformation. In order to obtain the joints' mechanical response in more detail, in situ micromechanical testing was conducted in the SEM chamber that allowed areas of 1x1 mm^2 and 50x50 mm^2 to be investigated.

The size of the welded region was rather small to be accurately captured from the camera based DIC system. Therefore a microscale investigation was pursued where the samples were tested within an SEM chamber. Low magnification SEM imaging was utilised in order to cover a viewing area of 1mm x 1mm while high magnification SEM imaging was employed to provide evidence of the occurrence of plastic deformation within the joint, at an area of just 50 μm x 50 μm. The strain evolution over the microstructural level, within the joint and at the base material was obtained. The local strains were highly non-homogeneous through the whole test. Final failure occurred approximately 0.2 mm away from the joint. Large local strains were measured within the joint region, while SEM imaging showed that plastic deformation occurs via the formation of strong slip bands, followed by the activation of additional slip systems upon further plastic deformation which end up in additional slip bands to form on the surface. Plastic deformation occurred by slip and twinning mechanisms. Upon

necking, significant out of plane deformations and slip deformation mechanisms were observed which suggested that plastic deformation was also happening at the last stages of damage evolution for the specific alloy. This was also evident from the large difference between the 600MPa UTS stress value and the low stress values before final failure (which in many cases was below 30MPa).

1. Introduction

Joining technologies have been intensively studied for over 70 years now, in many cases it is within the neighbourhood of the joints that engineering structures fail. It is due to the effect and alterations that these processes cause to the parent material that final failure may occur within, or close to the welded region. Microstructural changes to the parent material, such as grain growth and diffusion of elements to grain boundaries, as well as defects within the weld pool, like inclusions, porosity and lack of penetration, together with the development of residual stresses and (hot and cold) cracking within or close to the joint; all these mechanisms can lead to final failure of the component. At the same time due to the inhomogeneous high heat input and the level of constraint, distortion can occur in the final structure. Restricting the free movement of the component during welding, using a strong fixture, can minimise distortion, however may lead to an increase in the residual stresses [1-2].

Numerous joining processes have been developed due to the complex engineering geometries, interaction between the joining process and material behaviour, the use of new materials and technological developments (that have led to new joining processes). Processes such as laser welding, electron-beam welding, Gas Tungsten Arc Welding, Flux Cored Arc Welding, Gas Metal Arc Welding, Shielded Metal Arc Welding, Sub-merged Arc Welding and Resistance Spot Welding as well as Diffusion Bonded, Friction Stir Welding, and Self-Pierce Riveting and numerous others have been developed. All these processes allow engineers to join versatile types of materials, thicknesses and geometries [1-3].In the first family of joining processes, considerable amount of heating is generated in the material with high heating rates, and due to the fast inhomogeneous cooling rates in the nearbourhood of the weld combined with the low temperature of the base metal lead to distortions and residual stress development in the structure. Furthermore the properties in the welded region are much different from the base material and combined with the occurrence of defects in the joint (such as inclusions, cracks, and geometrical joint defects) may lead to stress concentrations at the welded region. In the later family of the processes relatively lower heating is generated at slower rates which decrease in return the cooling rates and minimises the residual stresses developed within the structure [1-2]. In this study the primary interest is on the joints made by diffusion bonding in thick sheets of stainless steel. This process has also the advantage of creating homogeneous microstructure between the base metal and the joint with minimum residual stress

development due to the slow cooling rates. Also no metal melting is necessary which minimises the possibilities for the creation of microstructural defects, such as pores and inclusions.

At the same time a lot of progress has occurred into assessing the mechanical properties of welded regions. Various authors have accessed the mechanical properties of the joints by means of hardness testing, Charpy V-notch, Crack Tip Opening Displacement, synchrotron and neutron diffraction, tensile, shear tests, bending tests, cyclic fatigue and creep [1-3]. However all these testing processes are limited to the size of the specimen. In welded structures, the corresponding regions of great interest, such as the Heat Affected Zone (the base metal that has been affected by the high heat input during welding), weld centreline or diffusion bonded area have small thicknesses, so assessing their mechanical performance is not possible via standard macroscopic mechanical testing techniques: tensile, fatigue, shear or CTOD testing. The corresponding areas where observations need to be made are too small. Small-sized specimens haven't been tested which could enable the characterisation of the mechanical performance of such small regions, areas and interfaces. Thus tensile testing of small sized specimens within an SEM chamber is performed in this study in order to access the Diffusion Bonded region of a joint between two stainless steel sheets. This study is of great importance in order to provide useful insights for more accurately modeling the corresponding regions.

Within the last 10 years, significant progress has occurred in terms of in-situ measuring the strain fields on the specimens by means of Digital Image Correlation (DIC) [4]. The main advantages of this technique is that it is contactless, results can be obtained at various difficult locations on the sample, and the resolution can be from kilometres down to the nanometre scale, depending on the image resolution and scale. DIC is a powerful technique that depending on the camera (lens) or the imaging technique used (photon based, electron based or X-rays), observations can be made at the scale of a large sample, down to the microstructure, within individual grains, defects and interfaces and even further down to individual atoms. A lot of studies lately have progressed towards the direction of qualitatively and quantitatively measuring the strain fields over the microstructure, at the micrometre scale [5-12]. This is made possible by inserting a small sized mechanical testing machine within the chamber of a SEM. By using such an approach it is possible to see the evolution of the microstructure during (thermo-) mechanical testing, evaluate damage nucleation and propagation at the very early stages, within microstructural features smaller to the grain size (precipitates, inclusions, interfaces). However all these studies are limited only in testing the parent material [5-12].

In this study a multiscale procedure was employed, where both camera-based and SEM-based experimentation were used. This was done in order to check for consistency in the mechanical properties of the joints. Three sets of samples were tested, in which the surface roughness of the two sheets was different (1, 3 and 9 μm), in order to evaluate the effect for the surface roughness of the two sheets on the mechanical performance of the corresponding joint. By employing a camera based DIC system a total of 39 tensile tests (21 along the Transverse Direction-Normal Direction and 18 along the Rolling Direction-Normal Direction) were performed and the stress-strain curves were obtained macroscopically. However it was not possible to measure whether final failure occurred away from the diffusion bond so a single in situ tensile test was done in the SEM chamber. By doing tensile testing within the SEM chamber it was possible to define where final failure occurred. Interrupting also the test at various stages during the tensile test, and taking two images at each stage, a macroscopic one (1mm x 1mm) and a microscopic one (100μm x 100μm), it was possible to correlate the macroscale phenomena (elastic deformation, plastic deformation, work hardening and necking) to the occurring microstructural evolution-deformation. Thus elastoplastic deformation and damage was evaluated down to the microstructural level. So the strains were measured at the whole sample, and also within individual grains. By using such an approach it was possible to capture where exactly final failure occurs with respect to the joint.

2. Experimental procedures

Two commercial grade 316L stainless steel plates - which initially had three distinct surface roughness (1, 3 and 9 μm) - have been diffusion bonded at 1050^0 C and 120MPa, for 2 hours. The two sheets had the same thickness of 7mm. An optically microscopy image was taken at the joint area and is shown in Fig. 1a. The diffusion bond can be distinguished as one of the sheets has the δ-ferrite precipitated along the Rolling Direction. The band contrast EBSD map is shown in Fig. 1b at the region of the diffusion bond, acquired via EBSD for 20kV and 240 mA aperture size. The phase shown with green colour is the δ-ferrite phase. The EBSD map was also used to obtain a better understanding of the microstructural features, such as grain size and shape, grain growth if occurred along the bond line and at the base steel sheets and grain orientation.

Tensile specimens were machined through the thickness of the joint in order to investigate the mechanical performance of the joint. 39 tensile tests were EDM machined in order to minimise the heat generated during machining and minimise the influence of machining on the actual microstructure of the supplied material. 18 samples were machined along the Rolling Direction and 42 samples along the Transverse Direction. The geometry and dimensions of the tensile samples is shown in Fig. 2.
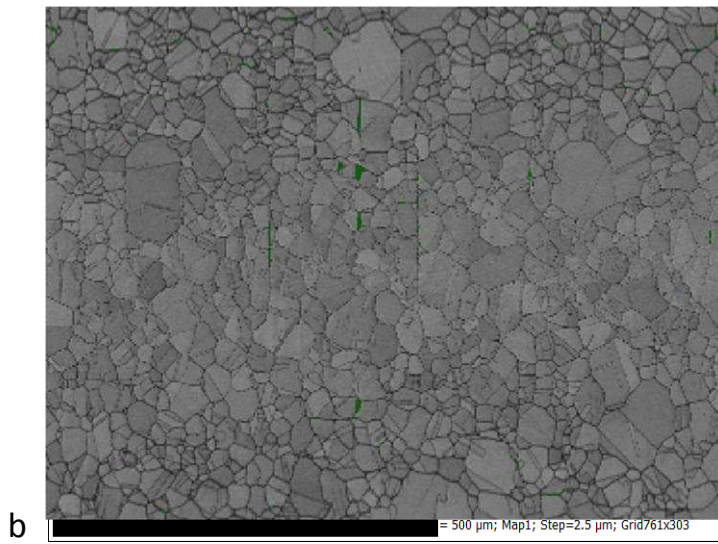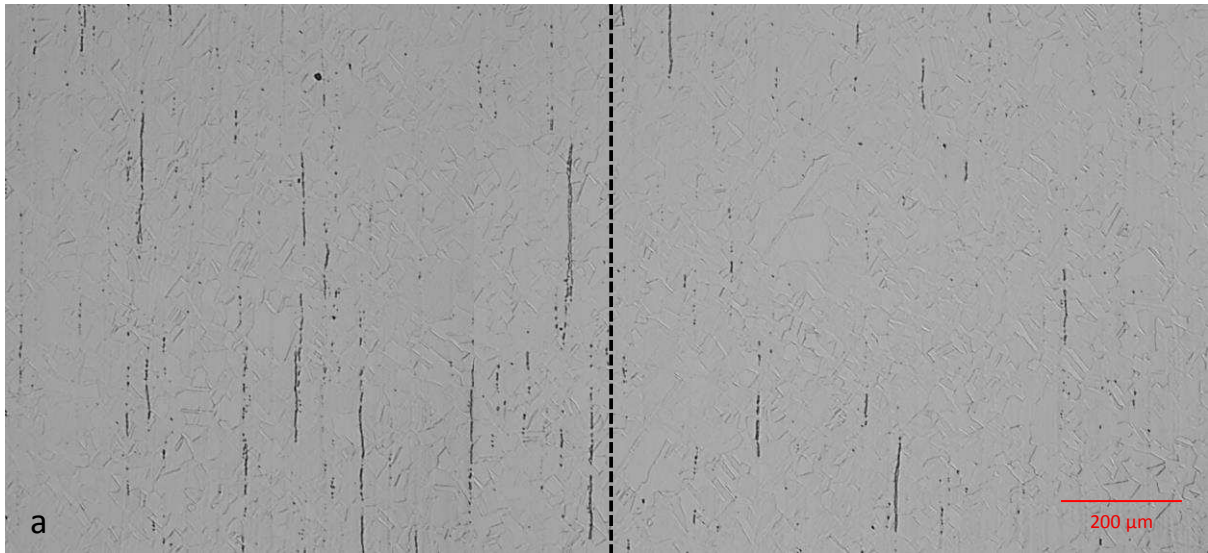
Fig. 1. a) Optical microscopy image of the microstructure of the two sheets within the region of the diffusion bond, b) EBSD map at the area of the joint.
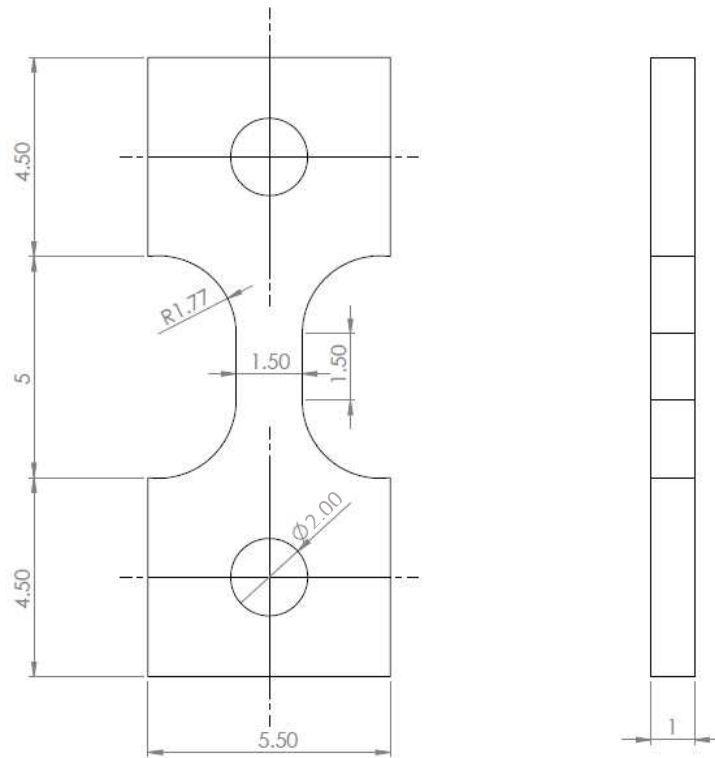
Fig. 2. Specimen geometry for room temperature tensile testing and b) Microstructure at the centre of the sample.

A 5kN capacity Gatan micro-mechanical tester, shown in Fig. 3 was used for all the tensile tests. A 12 MP (MegaPixel) 2D DIC (Digital Image Correlation) system was employed to acquire images of the specimen during testing. The images were used to calculate the displacements and the strains upon testing at the central area of the sample. The samples were initially painted with a black spray paint and then white-sprayed to create a white speckles over a black substrate and thus maximise the contrast of the image. The displacement of these white speckles was then utilised to measure the local strains. The samples were spray painted only at the gauge area, as the areas at the jaws needed to be kept clean. All tensile tests were conducted at room temperature, strain rate controlled conditions at speeds of 0.002 per minute up to yield point. After proof stress determination, speed was increased to 0.005 per minute. The DIC technique was capable of measuring the strains up to the UTS point. During necking, the paint speckles and therefore the image pixels were highly distorted due to the occurrence of high strains (above 100%). Therefore the stress-strain curves were obtained from the relative movement of the clamps. Due to the fact that the gauge length was small and most of the sample area was actually the clamped area small differences for the displacements should be expected between the strains at the actual gauge area (1.5mm x 1.5mm) at the centre of the sample and the displacements of the jaws. At last any slip at the clamps would have been observed in the images obtained by DIC analysis. The measured strains were obtained by

placing a virtual strain gauge at the central area of the sample as shown in Fig. 4. And the actual strain values were obtained in a plot as shown at the bottom of Fig. 4. From the plot the average value could be output and the macroscopic stress-strain curve was acquired.

A low magnification analysis (1500x) was initially used to ensure the selected area is a representative of the microstructure and evaluate the effect of phase distribution on local deformation and damage, followed by high magnification experiments (2800x) where the strain fields were acquired within the individual grains and phases. The corresponding micrographs cover an area of 79 μm × 54 μm, and 41 μm × 28 μm, consisting of approximately 15x15 and 7x7 grains, respectively; with the average grain size of 8 μm. The micrographs were analysed using the commercial image analysis software, DaVIS 7.2, by LAVision [10] to determine the in-plane displacement field from which the plastic strain values were calculated. The microstructural features of the material have been directly used as the correlating patterns for the images between two successive loading steps. A sensitivity analysis on the grid size was carried out, and a grid with 32x32 pixels was finally selected in all the experimental results presented in this study. Yet the results were consistent with a smaller grid as well; i.e. 16x16. A multi-pass algorithm [10] with 25% overlap between windows has been used to make the correlation work. A displacement accuracy of 0.01 pixels was obtained with a strain resolution of about 0.1% [10].
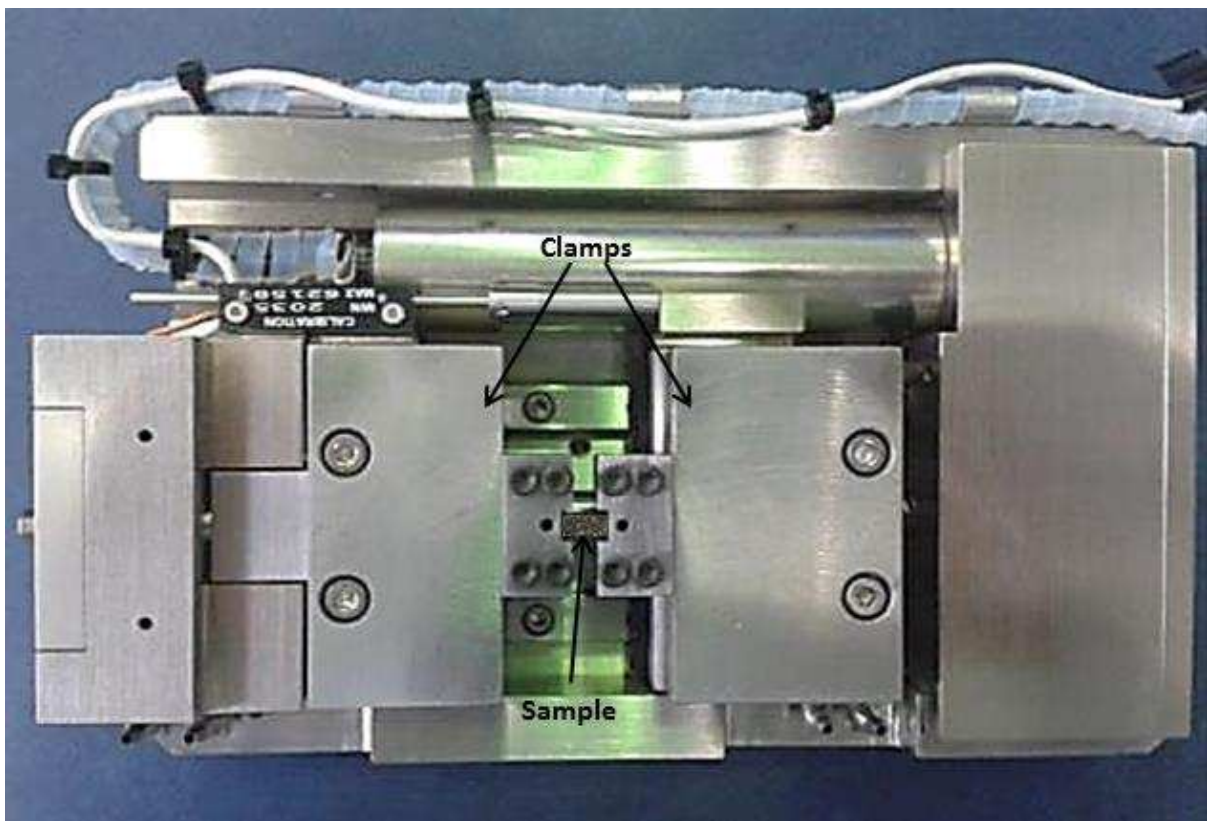

Fig. 3. 5kN capacity micro-mechanical tester, with a painted specimen clamped.
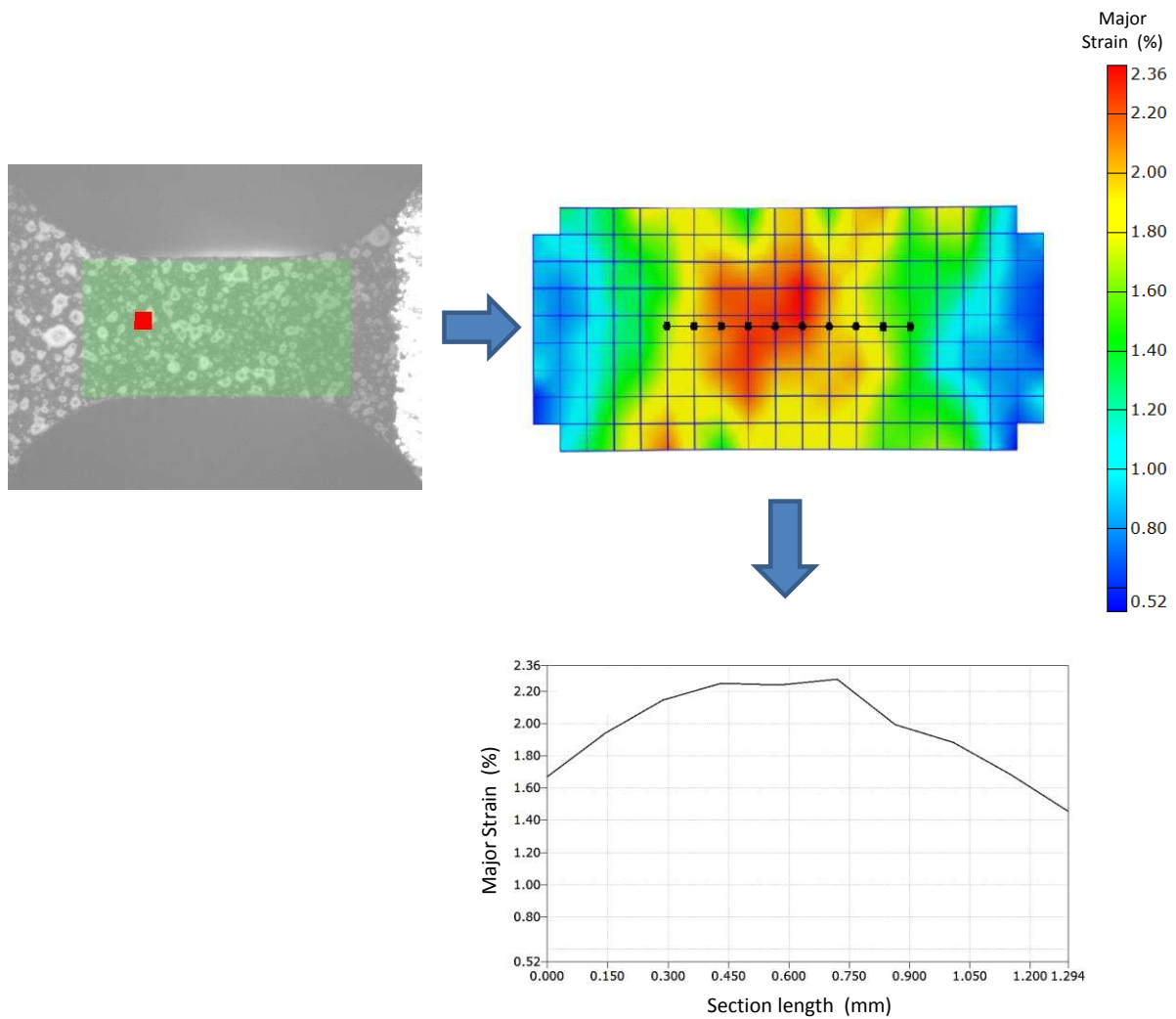
Fig. 4. Schematic diagram showing the process of gaining the strains at the central area of the sample by placing a virtual strain gauge. At the left top the sample image is shown captured by the DIC camera, overlaid is the masked area upon which the correlation occurs and the strain are measured. Next at the top right is shown the measured strains of the masked area along with a central line which corresponds to the virtual strain gauge. At the bottom image the strains at each point along the virtual strain gauge are obtained.

3. Experimental results

a. Macroscale characterisation of the mechanical performance of the joint

The stress strain curves for the three sets of tensile samples A, B and C can be seen in Fig. 5a-c. The curves for all the sets are similar for the elastic and plastic part. Deviations between the three sets of curves are observed only for the necking part of the curves. The surface roughness for the two sheets does not influence the elastic and plastic part for the curve in Fig. 5a-c. But there is a strong influence on the damage/ necking part of the curve. In general more deviations for the mechanical

properties are expected for the necking part of the curve with respect to the elastic part, plastic component and UTS point, due to the small size of specimen. Small deviations in the geometry of the specimen are expected to play a more important role for the necking part of the curve [13]. Furthermore the initial geometry of the crack formed in the sample varies depending on the location where it forms, the grain size, grain orientation within which it forms, the orientation of the neighbouring grains and the presence of micro-porosity (and micro-cracks) within the area of interest. All these effects cause alterations in the necking behaviour of the specimen and have been reported in literature [13]. Furthermore, in component design the application of such large strains should always be avoided. The applied stresses and strains are usually of the same order as the proof stress/strain. The deviations are negligible up to the UTS point.
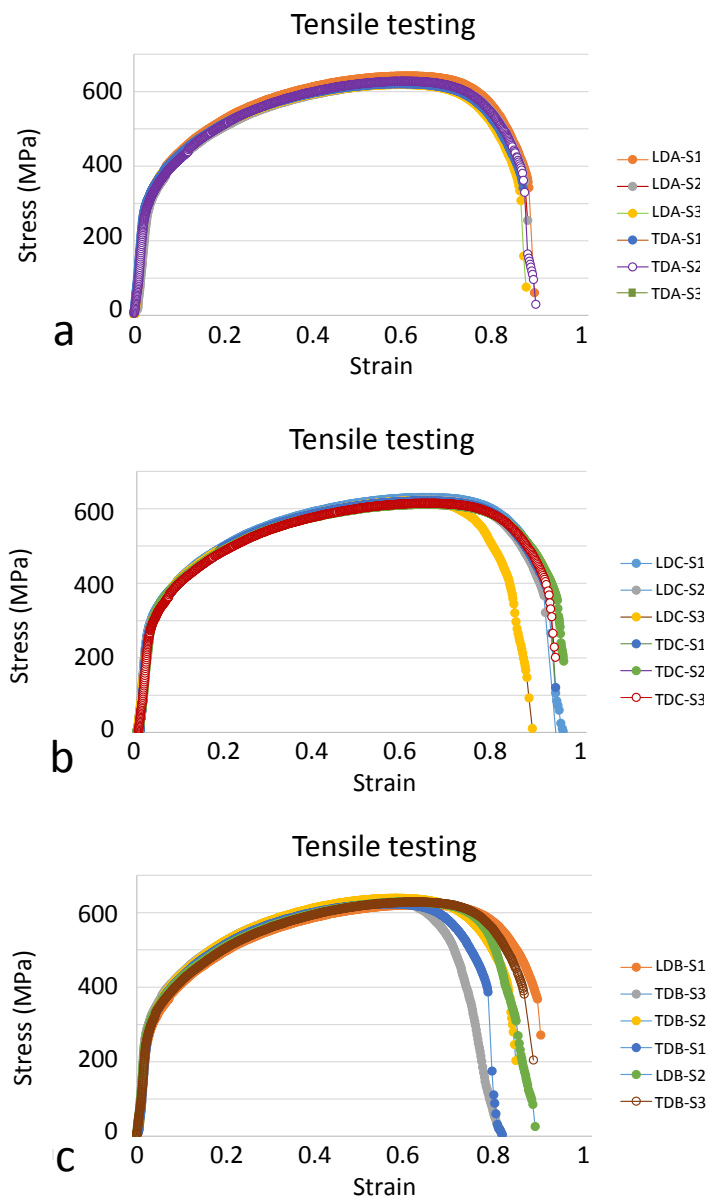
Fig. 5. a) Tensile test results for 6 samples, 3 along the LD and 3 along the TD for: a) Block A which corresponds to 1micron surface finish, b) for Block C which corresponds to 3 micron surface finish and c) for Block B which corresponds to 9 micron surface finish.

Table 1 shows the proof stress (0.2%), UTS point and total elongation for the three blocks; i.e. Block A, B and C. The average values for the proof stress, UTS point and total elongation are relatively close for all three blocks, with the highest deviation corresponding to the total elongation.

Average	Proof Stress (0.2%)	UTS	Total Elongation
Block A	312.22	627.38	0.82
Block B	322.35	630.02	0.80
Block C	315.25	620.62	0.79

Table 1. Average Material properties for the 3 Blocks.

In this section the DIC results are shown for the case study of Block B, sample 3 and along the TD. The strain development at the central area of the sample is shown during tensile testing at yield point (Fig. 5a), during work hardening (Fig. 5b) and at the UTS point (Fig. 5c). Fig. 5 shows the highly anisotropic behaviour of the material with the occurrence of high shearing as the strains have developed close to 45° angle with respect to the horizontal loading direction. Very high local strain values (0.9 at UTS point) were measured at the centre of the sample which provides evidence that the joints' properties are equal or better that the properties of the base metal. However it was not possible to clarify whether failure occurred exactly at the centre, which corresponds to the joint. Therefore a micro-scale approach was pursued where an EBSD map was initially taken at the centre of the tensile sample. This was done to evaluate the microstructure of the material at the joint but also to relate the final fracture line with respect to the location of the joint.
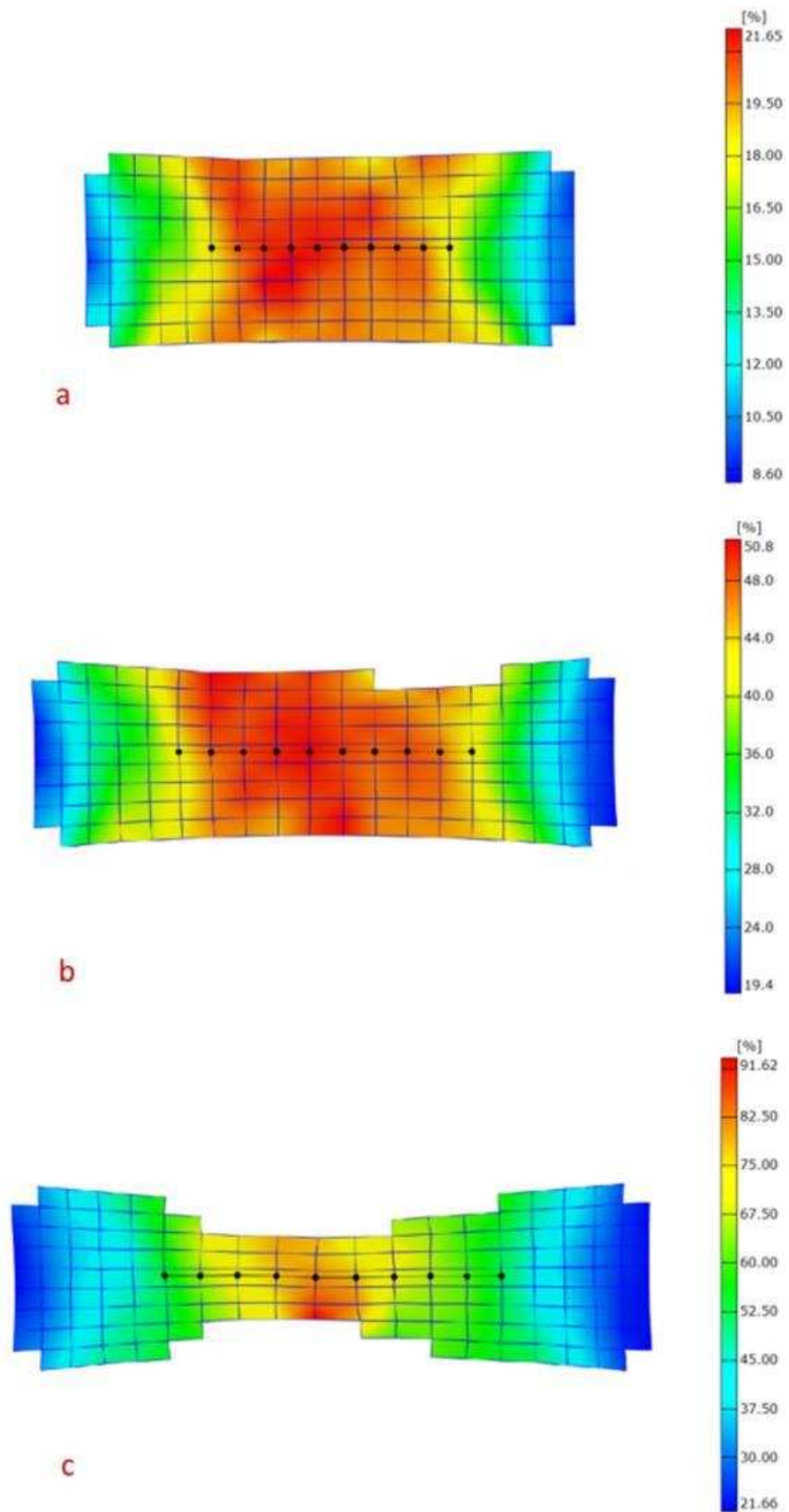
Fig. 5. DIC strain maps at the central area of sample 3, Block B. a) At yield point, b) during strain hardening and at c) UTS point.

b.   Meso- and micro-scale strain distribution

An EBSD map was taken to fully reveal the microstructure (grain size and orientation) at the centre of the sample. The joint area is small in thickness as the two sample surfaces are joined together via grain nucleation and growth. The joint area is shown at the centre of the sample with black dotted lines in Fig. 6. The yellow and orange boxed areas are the two areas inspected by SEM imaging during in-situ testing. The two magnifications selected, one low (200x) and one high magnification (3300x) are shown in Fig. 7 and correspond to the yellow and orange boxed regions of Fig. 6 respectively. The low magnification SEM imaging was selected in order to evaluate the strains at the 'macroscale' within a region of 1mm x 1mm and see the location of final failure with respect to the welded region while the high magnification SEM imaging was selected in order to investigate whether the joint plastically deforms or has a brittle micro-mechanical behaviour with respect to the base metal. These two magnifications are shown in Fig. 7.
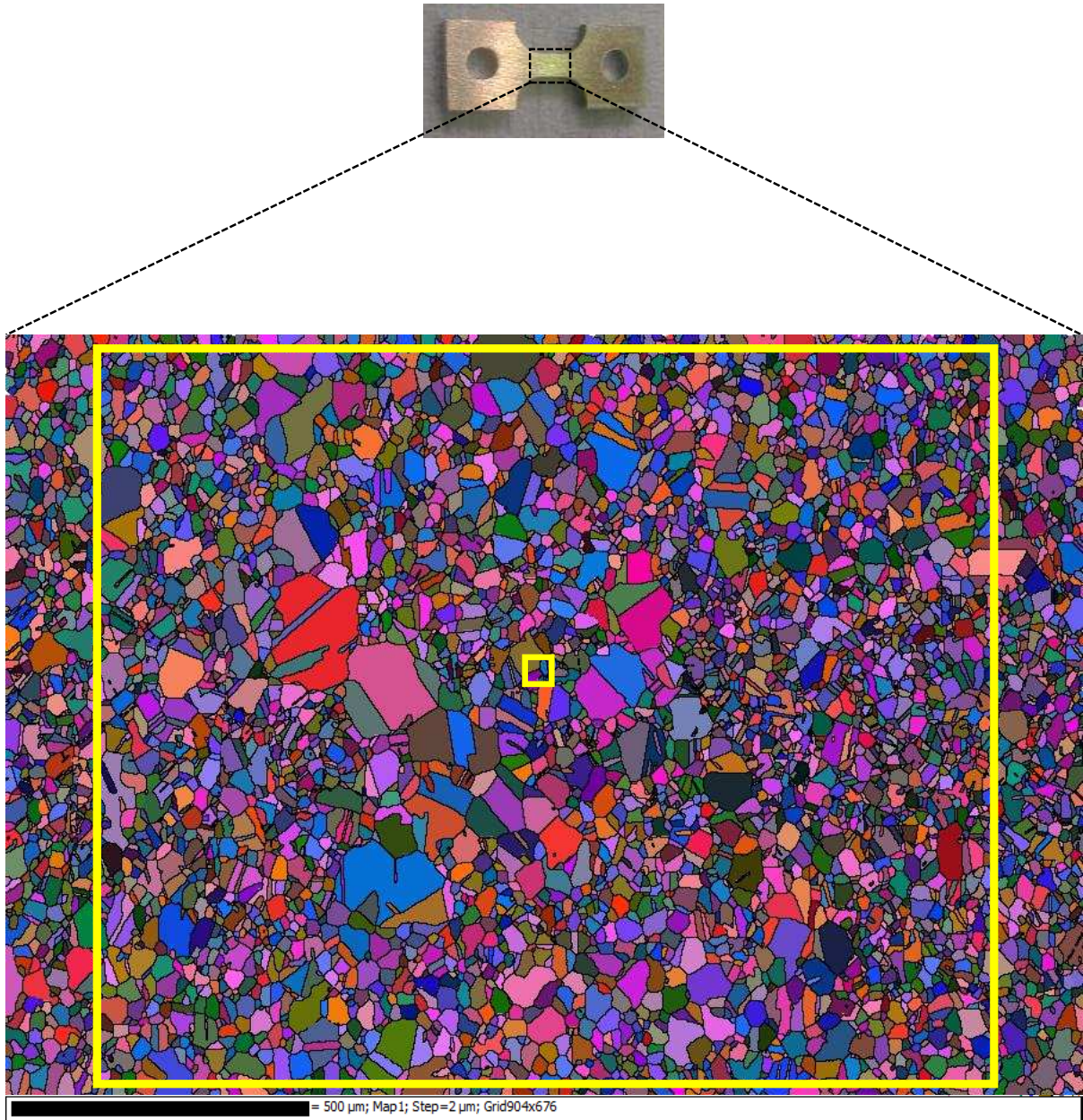
Fig. 6. EBSD map at the centre of the tensile sample. The two yellow-boxed areas correspond to the two SEM (imaging) magnifications which were used during in-situ testing. The small yellow-boxed area corresponds to an area within the joint, while the large yellow boxed region corresponds to the whole gauge area at the centre of the sample.
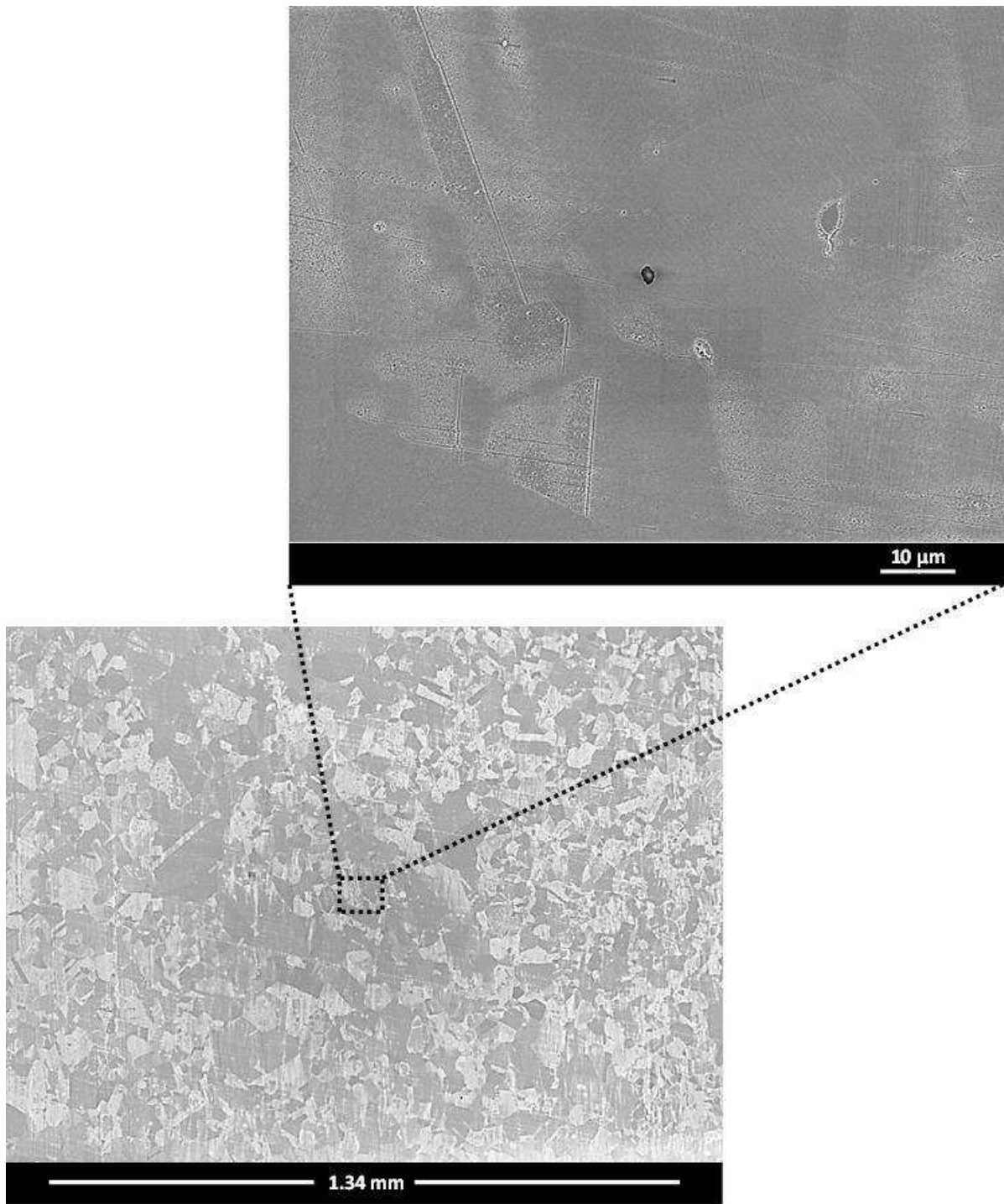
Fig. 7. Low and high magnification SEM images selected for this study. The low magnification image was selected to obtain the 'macroscopic' strain fields at the joint region and the high magnification image provides evidence of the ductility of the corresponding material at the joint.

Fig. 8 shows the stress-strain curve and the location (the corresponding stress and strain) upon which the test was interrupted to take SEM images in order to correlate the macroscopic boundary conditions with the evolution of the microstructure. At this stage the tensile test was interrupted after the elastic region of the stress-strain curve (Fig. 8a), at the beginning of plastic deformation.

Once the test was interrupted, a low and a high magnification image were taken. In Fig. 8b, a high magnification image is shown (x3200) and on the surface it can be observed that slip bands have formed in some grains. The black, red and white arrows correspond to slip bands, twins and an inclusion site. Twins in some cases can be seen depending on the crystallographic rotation. Yet most twins cannot be seen by SEM imaging. In Fig. 8c the low magnification image (x200) is shown. The local strain distribution is shown over the microstructure, obtained by means of DIC. The occurrence of long shear bands can be seen at this stage. The angle of the shear bands vary depending on the local microstructure. All shear bands are close to 45° with respect to the loading direction.

So at the macroscale, the sample has shear bands extended over several grains. At the same time at the microscale slip bands form within the grains, localising the strains. These slip bands are constrained within the individual grains. However the individual slip bands form within individual crystals and extended across the full length of the crystal matrix. The acting shear at the corresponding grain boundaries, activate the slip bands at the neighbouring grains forming the macroscopically observed shear bands. Fig. 9 corresponds to an applied strain of 0.45 (approximately 65% of the total plastic deformation has been applied to the sample). New slip bands form within more grains than in Fig. 8b. The slip bands are wider with respect to Fig. 8, as more and more dislocations exit the sample at the free surface at higher global strains. In some cases the slip bands cross each other in a rather vertical angle as shown with the yellow arrow, reducing significantly dislocation slip. At the same time more twins (green arrows) have formed increasing the work hardening (and the stress levels of Figs. 8a and 9a), as the global strains increase. The excessive plastic slip has led to shear failure at the red-arrowed location. No void growth occurred at the inclusion site, suggesting that the presence of inclusions does not influence the macroscale and microscale mechanical performance of the alloy. Fig. 10 corresponds to the macroscopic UTS point. Stronger and wider slip bands form in Fig. 10d as the material work hardens. The spacing between parallel slip bands has also decreased significantly. Dislocations become blocked within the slip bands as the slip bands are crossed by other slip bands. Through the images of Figs. 8c, 9c (as well in Figs. 10c and 11c) there is no excessive void growth at the inclusion site, suggesting that damage is constrained at the inclusion site by the surrounding ductile matrix.

The length of the shear bands decreases at higher global strain and this can be seen by comparing the lines drawn over the DIC strain maps in Figs. 8 and 9. However more shear bands have formed in Fig. 9. The strains are highly localised in both DIC strain maps. No strain partitioning is found in both maps that suggests that the micro-mechanical performance of the base metal and the joint-area are similar.
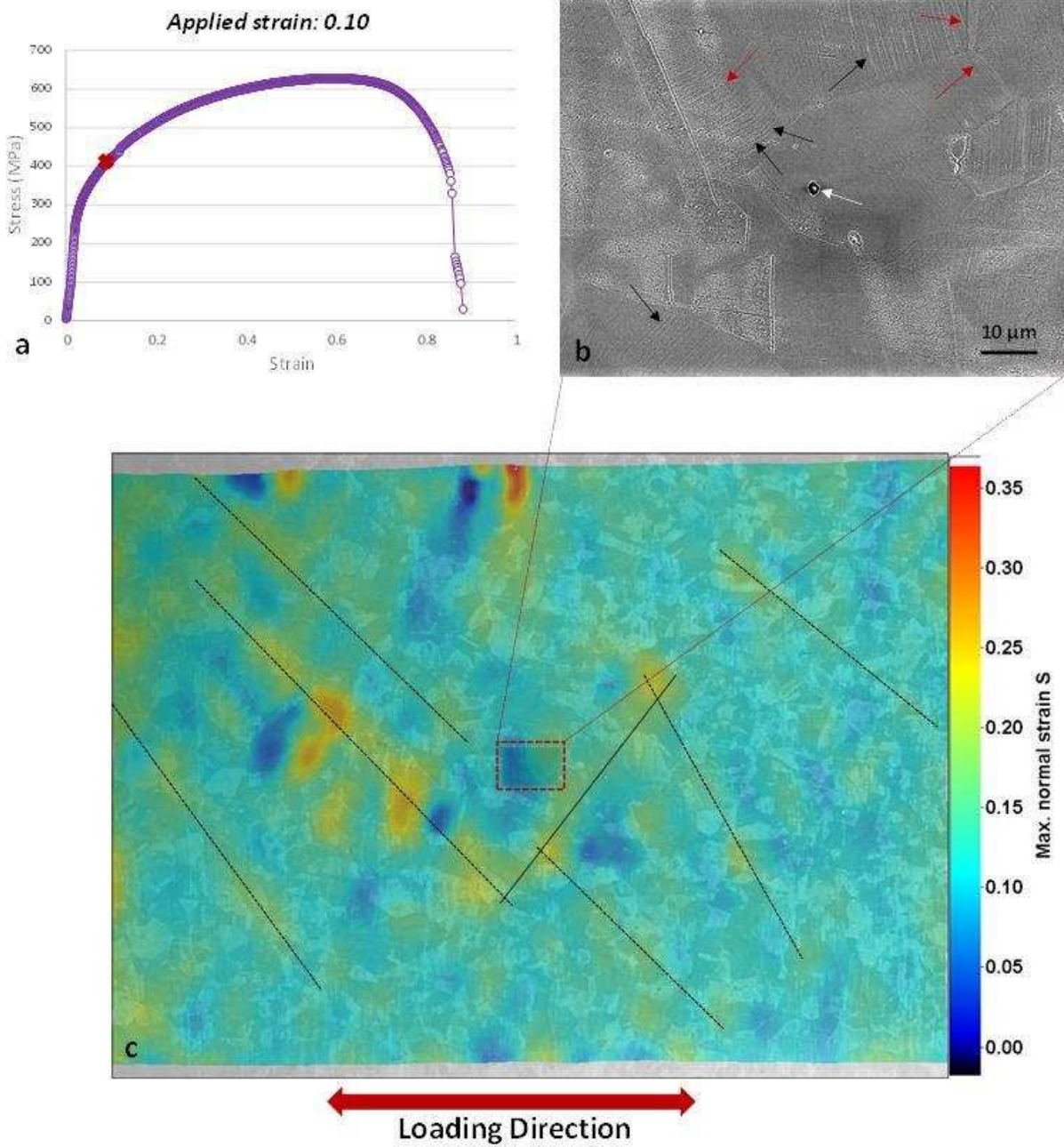
Fig. 8. a) Applied strain of 0.10; onset of plastic deformation. b) The deformed microstructure within the weld. c) The strain distribution for the sample for a nominal applied strain of 0.10.
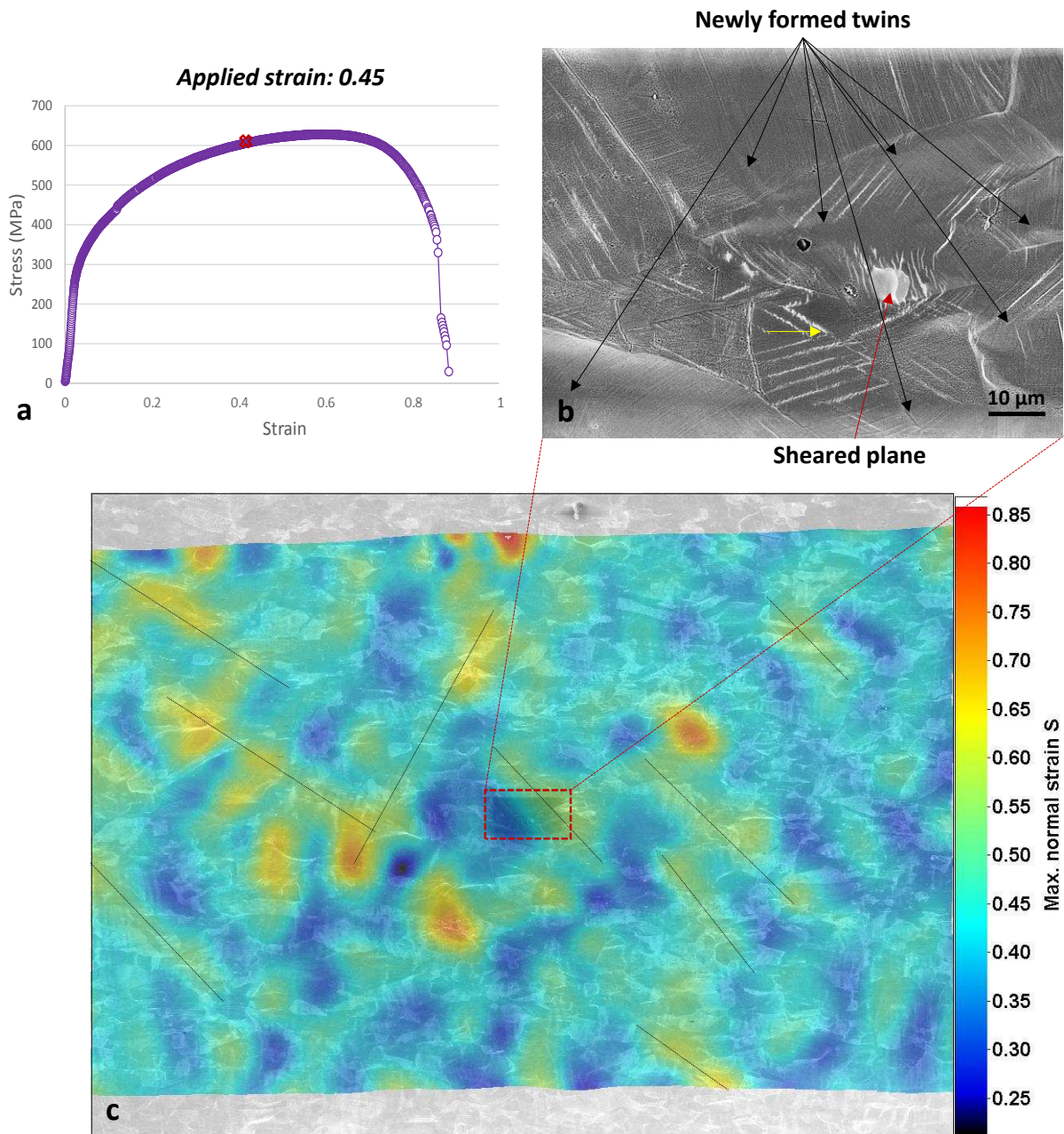
Fig. 9. a) Applied strain of 0.45. The location corresponds to allocation starts to saturate as it approaches the UTS point. b) The deformed microstructure within the weld. c) The strain distribution for the sample for applied strain of 0.45.

A dense network of strong slip bands has formed in all grains for an applied strain corresponding to the macroscopic UTS point (see Fig. 10a and b). In several cases, the slip bands are tangled at a rather vertical angle, restricting significantly dislocation movement and glide. For the grain where the inclusion is also located, the distance between parallel neighbouring slip bands has decreased significantly, employing all the plastic deformation capabilities of the crystalline matrix within the heavily deformed grains. While other grains at the top and bottom of Fig. 10b, do not have the same

density of slip bands and therefore do not have the same contribution to the macroscopic plastic deformation. This is due to the plastic anisotropy and local orientation of the individual crystals. At Fig. 10c, the highest values for the major strain are localised at the black circled area of the DIC strain map which provides an indication of the location where necking will occur.
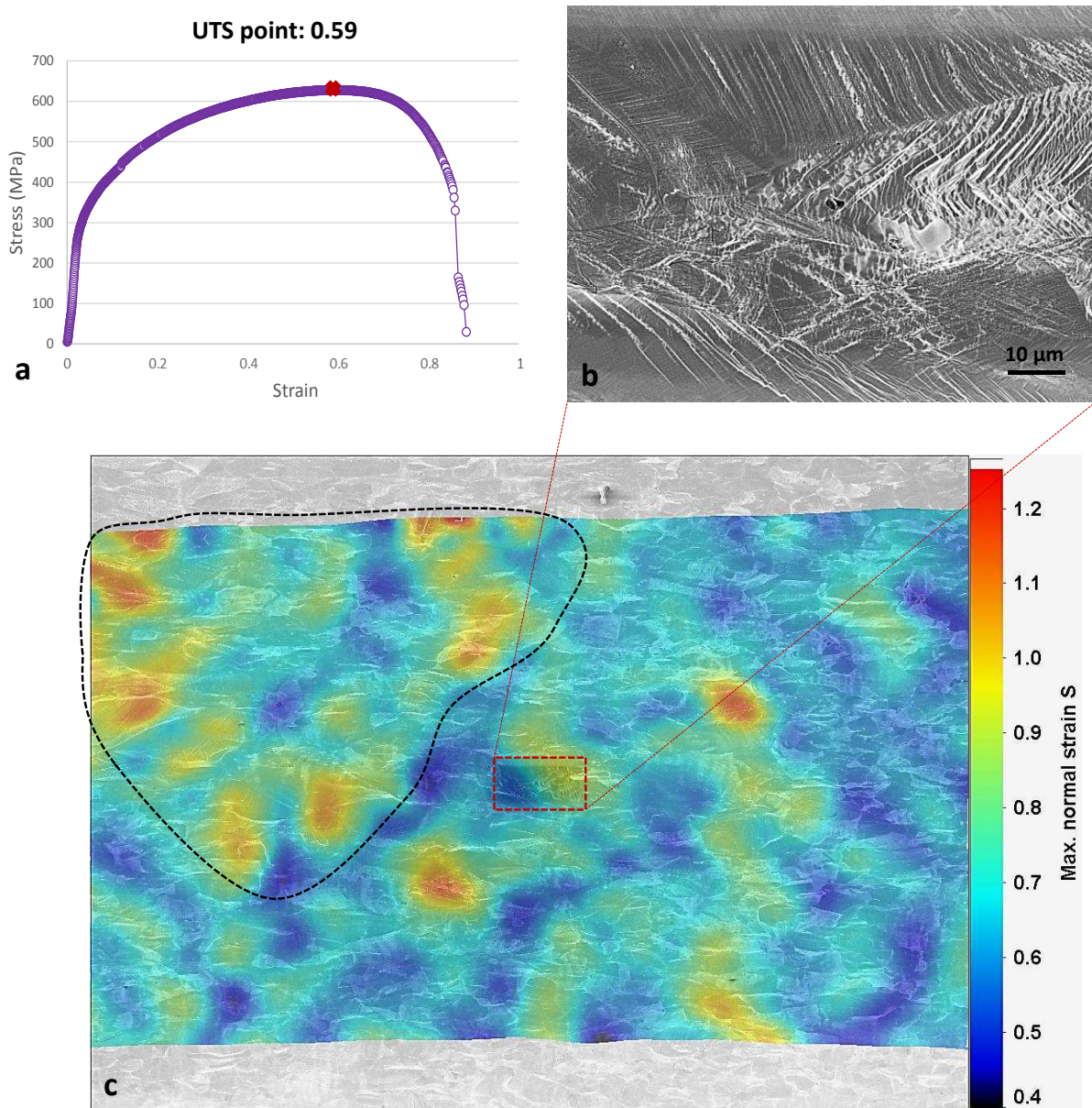

Fig. 10. a) Applied strain of 0.59; UTS point. b) The deformed microstructure within the weld. c) The strain distribution for the sample at the UTS point. The maximum strains are highly localised within the black-boxed area.

Fig. 11 corresponds to a macroscopic strain of 0.8, which lies within the necking area of the stress-strain curve in Fig. 11a. The slip band distribution in Fig. 11b has not changed significantly with respect to Fig. 10b. This is because necking occurs far from the inspected/joint area. Necking

occurred at the black-circled and red-circled regions of Figs. 10c and 11c. The strains have increased significantly within the necking area, while strain relaxation occurs at the right side of Fig. 11c (if compared with the right side of Fig. 10c). The DIC measured strain distribution (0.5 up to 2.25) is much higher than the average strain value at the stress-strain curve of Fig. 11a, which is due to the damage that has occurred within the necking area. Damage nucleation and evolution takes place and the DIC software is not capable to differentiate between plastic deformation and damage nucleation, crack formation and propagation [4, 5, 10].
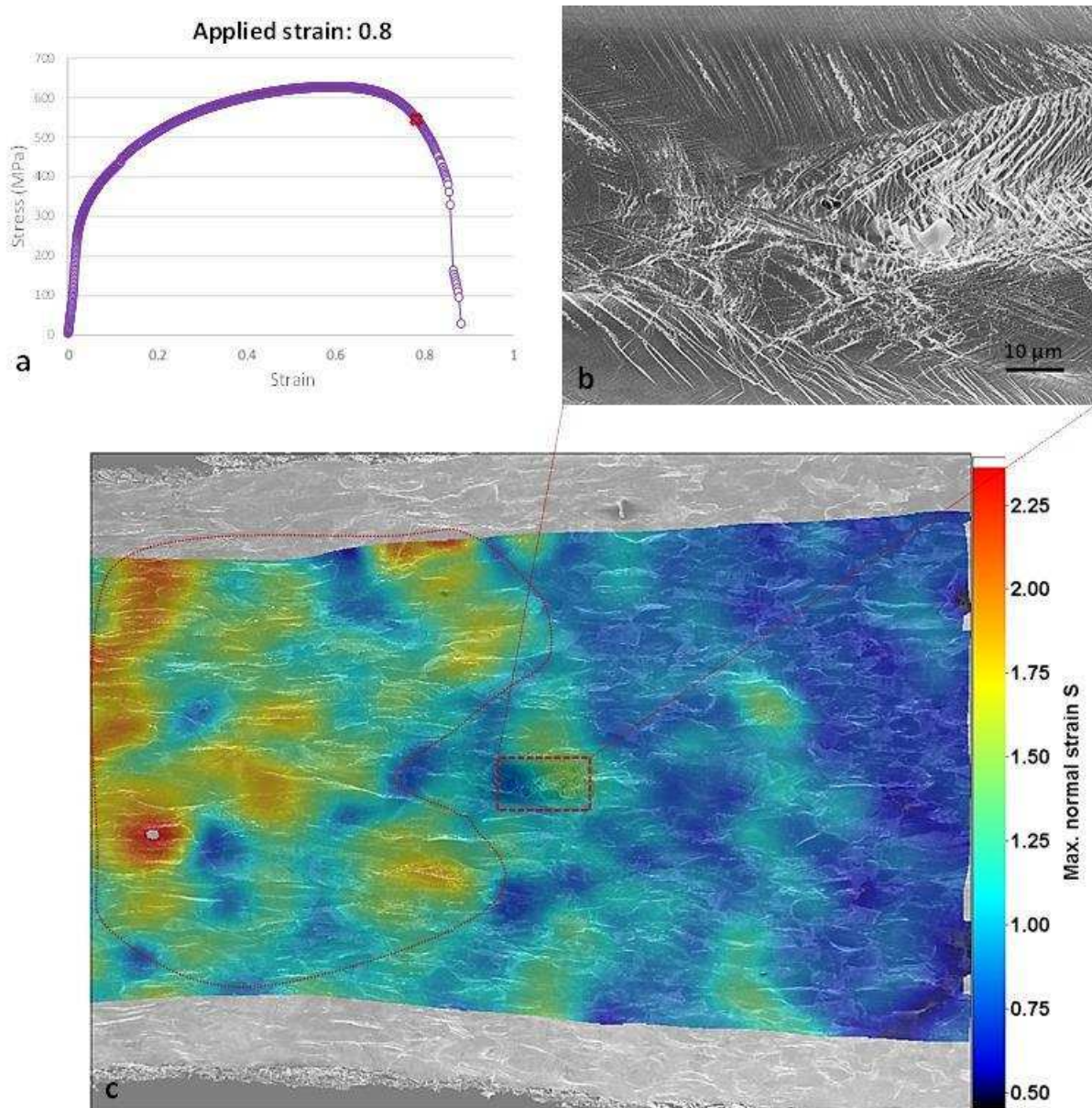

Fig. 11. a) Applied strain of 0.8; within the necking part of the stress-strain curve. b) The deformed microstructure within the weld. c) The strain distribution for the sample upon necking. Within the red circled area the maximum strains occur, indicating the location of final failure.

c.   Assessment of final failure

Initiation of necking and final failure was captured by means of low magnification SEM images. The final stress value just before final failure was reasonably low, with an engineering stress value of just 25MPa, signifying the ductility and the amount of necking of the alloy. By comparing Fig. 12a and d, a total necking of 30% has occurred with respect to the original sample width. The final fracture line was obtained by observing the deformation of the microstructure throughout the test. Fig. 13 shows as a white-dotted line the fracture line and with black dotted lines the region of the joint. Both areas are shown on the EBSD map and it can be seen that the final fracture line is several hundreds of micrometres away from the joint area, varying between 150 and 400μm. The cracking had a transgranular nature due to the origins and the accumulation of plastic deformation which occurred along slip bands and individual crystal slip systems.
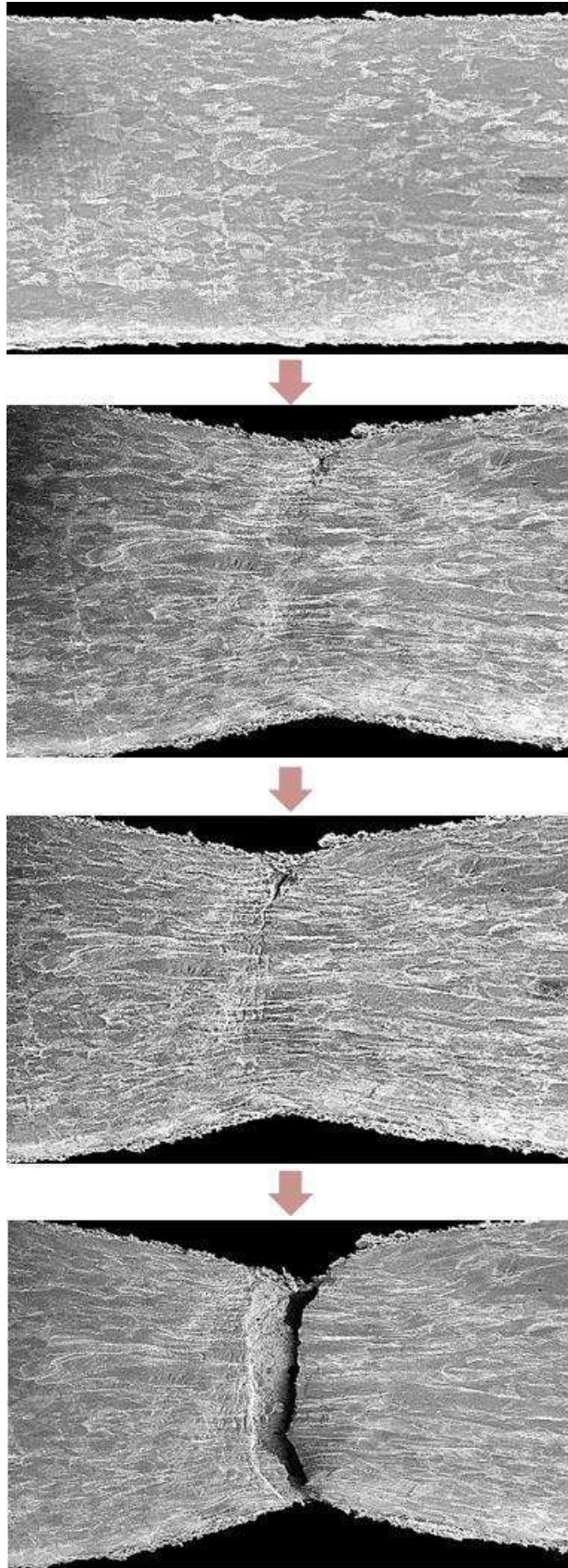
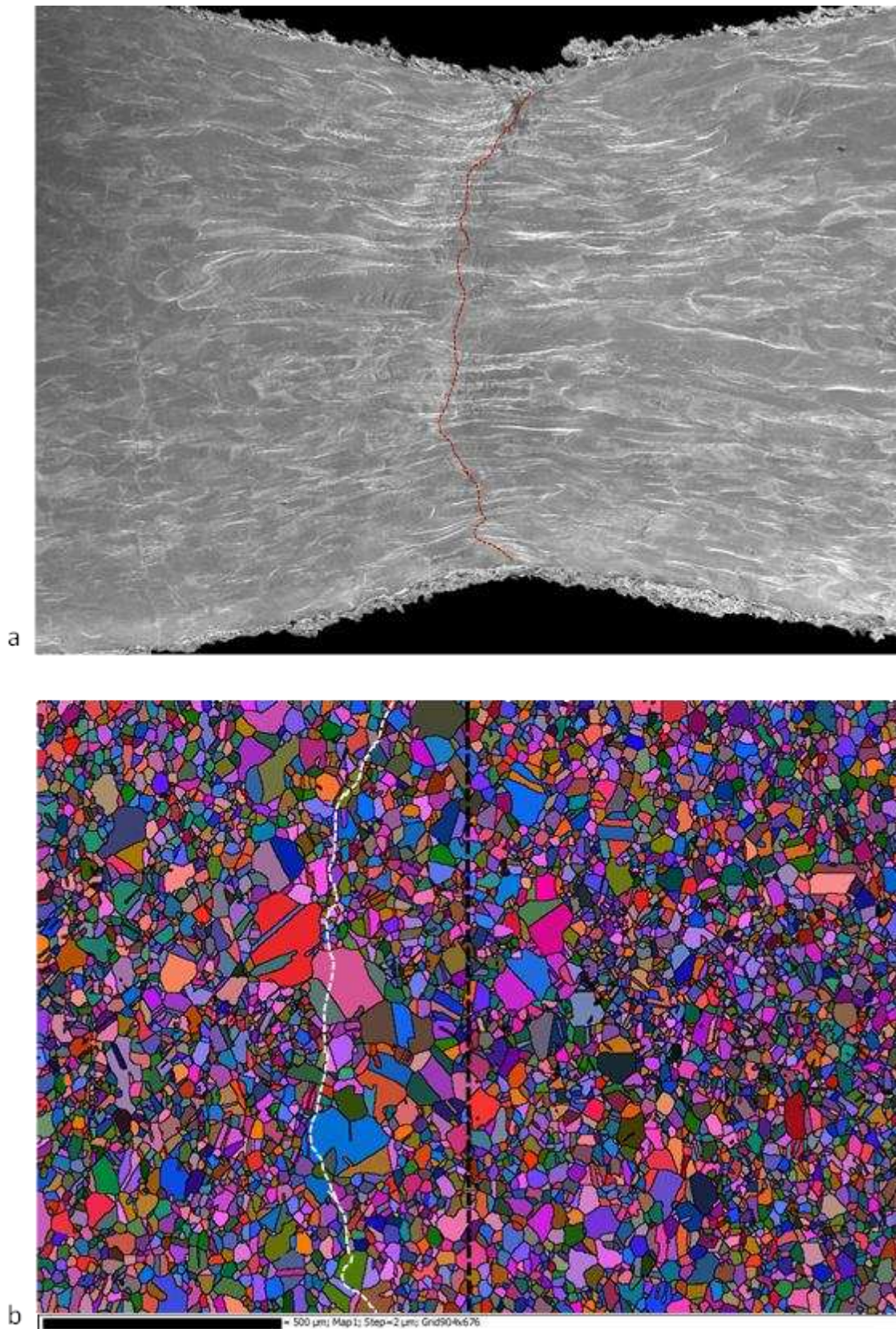Fig. 12. Necking, crack initiation and final failure during tensile testing.

Fig. 13. a) The necked sample is shown at the onset of crack nucleation. The location of the fracture line is superimposed as a red dotted line, b) the position of the fracture line is overlaid on the EBSD map for the undeformed sample. The fracture line is 150-400µm away from the joint.

4. Discussion

Macroscopic DIC coupled tensile tests were performed to obtain the global and local stress-strain fields. Large strains were measured by means of DIC, signifying the ductility of the alloy. All the stress-strain curves were similar for all the specimens up to the UTS point while differences were found only for the necking part of the curve. These differences can be attributed to the location where crack nucleation occurred, the grain size, grain orientations, local misorientations and crack growth resistance of the neighbouring grains within which the crack has to propagate. The presence of voids and inclusions and their distribution as well affect damage nucleation and evolution. All these factors have strong interactions, which lead to large variabilities in the necking component for the curve. However in this study, the interest lies primarily to the elastic and plastic part of the curve, and therefore the performance of the sample during necking was neglected. For the local DIC measured strain fields, no alterations or strain localisations were observed at the centre of the samples, where the joint is. Yet the joint area is too small to be able to observe any influences that the joint can impose to the local stress-strain fields.

Therefore in situ micro-mechanical testing was performed at two distinct magnifications (Figs. 6 and 7) in order to capture the global strains over a large area of 1mm x 1mm and the local strains within the joint. Furthermore the high magnification images revealed the microstructural deformation characteristics of this alloy, the formation of slip bands and twins. At the first stages of plastic deformation in Fig. 8 distinct slip bands formed within the grains, at the corresponding critical slip systems which were close to a 45^0 angle between the loading axis and the orientation of the slip bands. The spacing between these bands within the grain was large enough that any interaction can be ignored initially. Also the formation of twins was captured within some grains depending on the crystal orientations. Yet in situ EBSD measurements during tensile testing was not employed to accurately measure the evolution of twinning as the purpose of this study was to reveal the mechanisms of plastic deformation and the mechanical performance of the joint. So evaluating the local strain fields by means of DIC was set to be of great importance.

Upon progressive straining of the sample, the number of slip systems and slip bands that are activated increases. Figs 8 and 9 show that the spacing between the initial slip bands within each grain decreases significantly and their interaction therefore starts to play a role. Cross linking occurs between the initial slip systems and the secondary ones. This in turn minimises significantly the distances upon which the dislocations can move, reducing the possibility for further plastic deformation of the alloy.

The length of the shear bands which extend through several grains, decreases through Figs. 8c and 9c. This is due to the fact that more slip systems are activated at different angles blocking further plastic deformation at the initially formed slip bands. Furthermore extensive work hardening has occurred within the initially formed strong slip bands. In Fig. 10c the number of shear bands has further increased but their corresponding lengths has reduced.

In Figs. 10 and 11, the slip bands become wider and more and more slip bands are cross linked with other slip bands. The deformation and damage mechanisms in this alloy are governed by the activation and evolution of the corresponding slip systems and twins; and the behaviour of inclusions does not influence strongly the macroscopic mechanical performance of the alloy.

There are no significant differences between the high magnification images, as necking occurs but in a few micrometres away from the joint. The low magnifications images reveal the location where strain localisation occurs initially which leads to necking, crack nucleation which is captured in Fig.14b and final failure as the crack runs through the sample in Fig. 14c.

The final failure is away from the joint, signifying the tolerance of the joint. Images were also taken at the area of failure throughout the test, where significant plastic deformation was found to occur, by means of slip bands formation. This suggests that final failure occurs at a location were initially significant plastic deformation occurs. All these observations made in this work show the sound mechanical properties of the joint, the significant work hardening of the sample at the joint area, neighbourhood of the joint and base metal.

5. Conclusions

The diffusion bond between two blocks of stainless steel 316L has been tensile tested for three blocks with the joint at the centre and to understand the stress-strain behaviour and the macro/micro deformation response. The central area of the samples containing the joint shows highly anisotropic behaviour which could be due to the formation of dislocations and twinning. Between the relatively low yield stress (~315MPa) and high UTS point (~626MPa), considerable work hardening occurs, which allows the material to be deformed up to very high strains (more than 90%) before necking starts. The extended deformation capabilities can also be seen by the low engineering stresses and the difference between the UTS stresses and the engineering stresses just before final failure.

The strain evolution showed no strain localisation at the area of the joint with extensive shear straining and work hardening spread over all the gauge area of the sample, which is related to the material properties of stainless steel 316L.

References

1. G. den Ouden *Lastechnologie*, Delftse Uitgevers. Maatschappij, Derde druk 1993.

2. Welding Handbook, 8th Edition, Vol. 1 Welding Technology. American Welding Society, Miami, 1987.

3. Welding Handbook, 8th Edition, Vol. 2 Welding processes, American Welding Society, Miami, 1991.

4. Image Correlation for Shape, Motion and Deformation Measurements: Basic Concepts, Theory and Applications. Michael A. Sutton, Jean-José Orteu, Hubert Schreier – 2009

5. P. Efthymiadis, PhD thesis, Multiscale Experimentation and Modeling of fatigue crack development in aluminium Alloy 2024, The University of Sheffield, 2015.

6. Avramovic-Cingara G, Saleh CAR, Jain MK, Wilkinson DS. Metall Mater Trans A 2009;40A: 3117.

7. Kadkhodapour J, Butz A, Ziaei Rad S, Schmauder S. Int J Plasticity 2011;27:1103.

8. Kang J, Ososkov Y, Embury JD, Wilkinson DS. Scripta Mater 2007;56:999–1002.

9. Maire E, Bouaziz O, Michiel MD, Verdu C. Acta Mater 2008;18:4954–64.

10. Ghadbeigi H, Pinna C, Celotto S, Yates JR. Mater Sci Eng 2010; 527A:5026–32.

11. Tasan CC, Hoefnagels JPM, Geers MGD. Scripta Mater 2010; 62:835–8.

12. Avramovic-Cingara G, Ososkov Y, Jain MK, Wilkinson DS. Mater Sci Eng 2009; 516A:7–16.

13. SA Soberanis, PhD thesis, 3D CAFE modelling of ductile fracture in gas pipeline steel. PhD thesis, The University of Sheffield, 2007.